Supporting Information

Flexible freestanding all-MXene hybrid films with enhanced capacitive performance for powering flex sensor

Zhemin Li, [a] Yohan Dall'Agnese, [b] Jin Guo, [a] Haifu Huang, [a] Xianqing Liang [a] and Shuaikai Xu*[a]

[a] *Guangxi Colleges and Universities Key Laboratory of Novel Energy Materials and Related Technology, Guangxi Novel Battery Materials Research Center of Engineering Technology, Center on Nanoenergy Research, College of Physics Science and Technology, Guangxi University, Nanning 530004, P. R. China*

[b] *Institute for Materials Discovery, University College London, London WC1E 7JE, United Kingdom*

Dunn's differentiation method

The current response at a fixed potential of the electrode materials can be expressed as being the combination of two separate mechanisms, surface capacitive effects and diffusion-controlled insertion processes.

$$i(V) = k_1 V + k_2 V^{1/2}$$

For analytical purposes, we rearrange this slightly to

$$\frac{i(V)}{V^{1/2}} = k_1 V^{1/2} + k_2$$

$k_1 V$ and $k_2 V^{1/2}$ correspond to the current contributions from the surface capacitive effects and the diffusion-controlled intercalation process, respectively. Thus, by determining k_1 and k_2, we are able to quantify, at specific potentials, the fraction of the current due to each of these contributions. The detail procedures to evaluate the $C_{capacitive}$ and $C_{diffusion}$ are as follows.

(1) Collect the cyclic voltammograms at various scan rates, including very slow scan rates (<20 mV s^{-1}).

(2) Fix a potential and read the current from different cyclic voltammograms, as shown in Fig .S1.

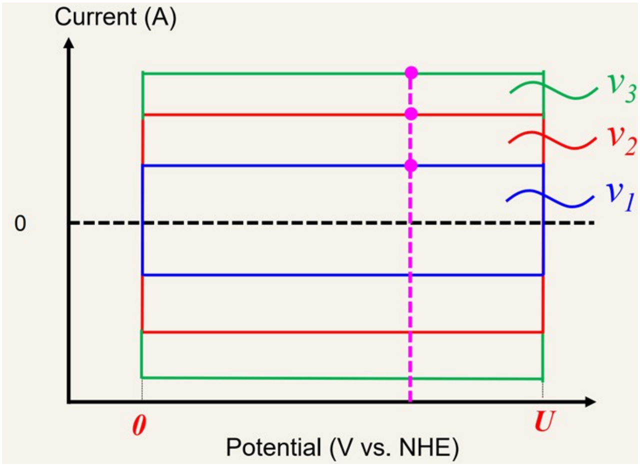

Fig .S1

(3) Plot the lines $\frac{i(V)}{V^{1/2}}$ vs. $V^{1/2}$. The k_1 and k_2 are the slope and y-intercept, respectively.

(4) Differentiate current at a certain scan rate, as shown in Fig. S2.

(5) Repeat step (3)-(4) for other potentials.

(6) Evaluate $C_{capacitive}$ and $C_{diffusion}$.

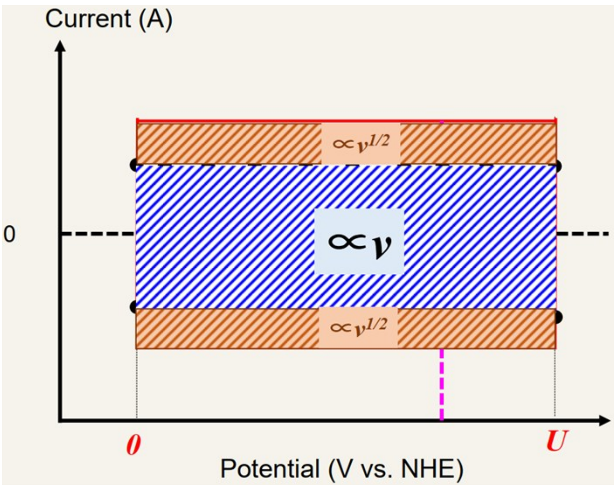

Fig. S2

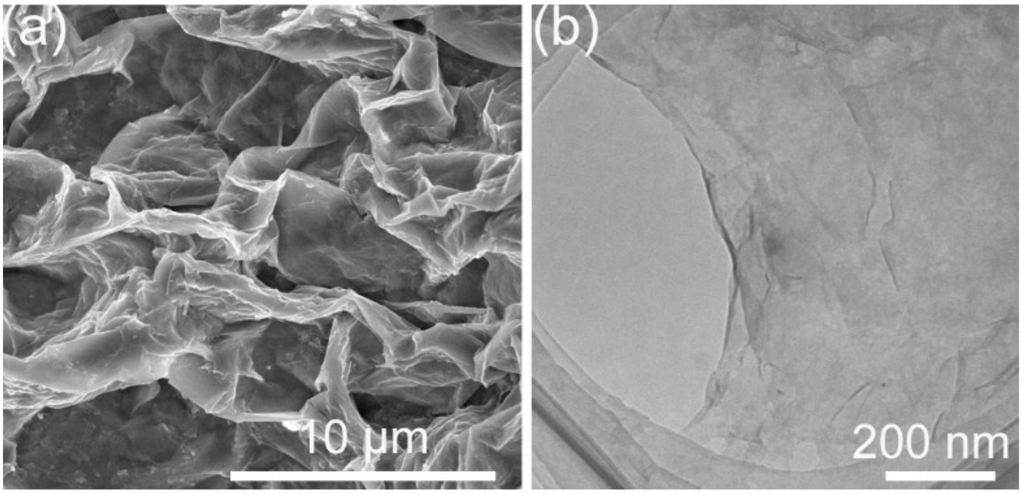

Fig. S3. The SEM image (a) and TEM image (b) of the prepared few-layer $Ti_3C_2T_x$ nanosheets.

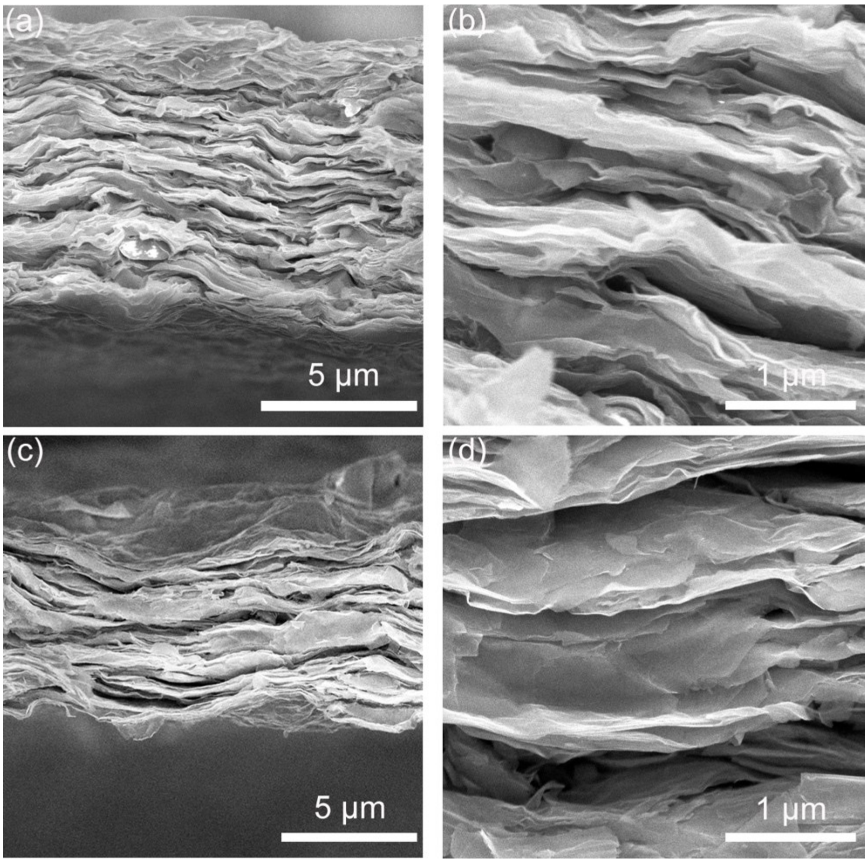

Fig. S4. (a) Cross-sectional SEM image of the pure Nb_2CT_x film. (b) The high magnification SEM image of (a). (c) Cross-sectional SEM image of 50% T-N film. (d) The high magnification SEM image of (c).

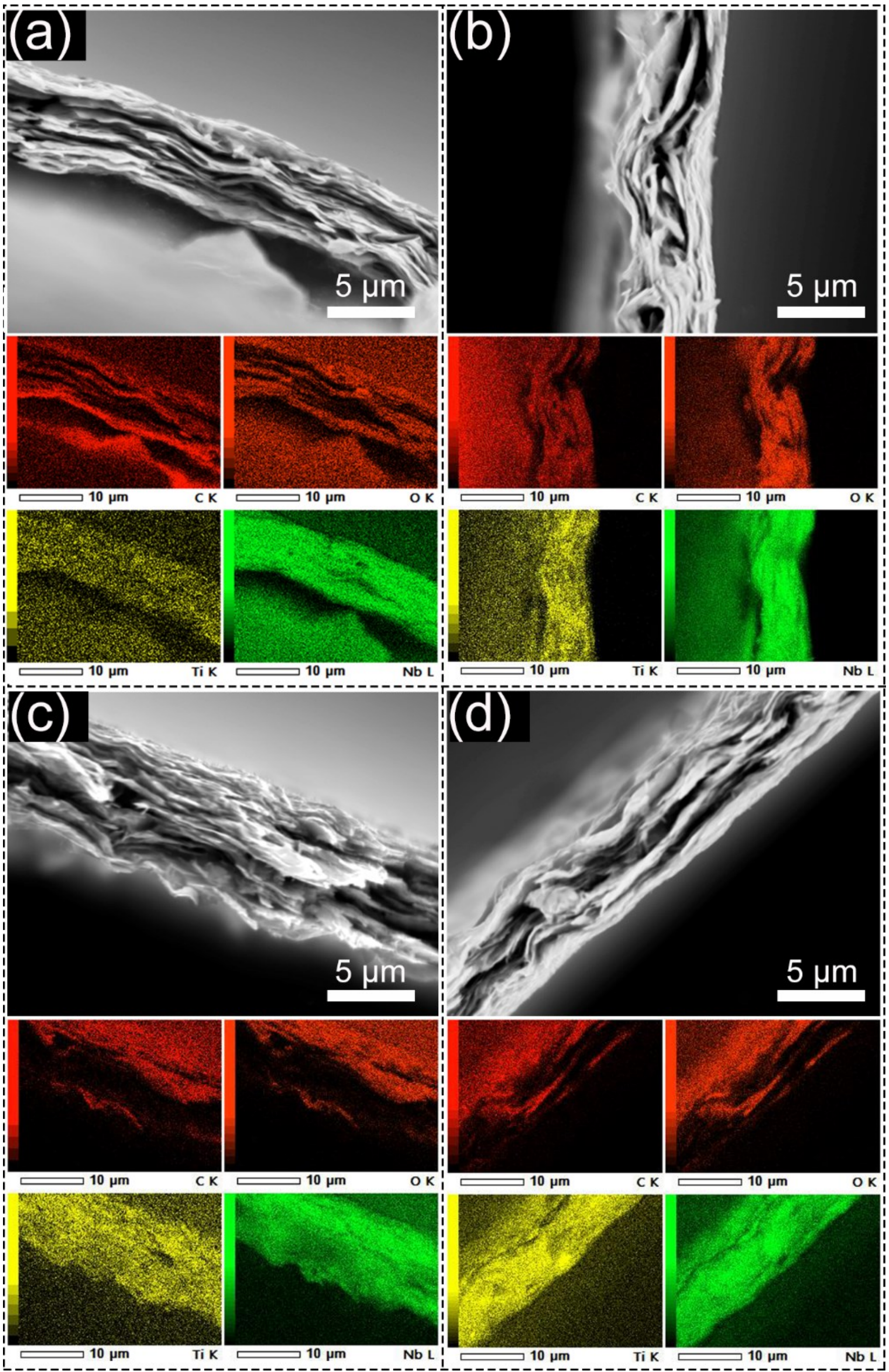

Fig. S5. EDS mapping images of the cross-sectional views of all-MXene films (a) 5% T-N, (b) 10% T-N, (c) 30% T-N and (d) 50% T-N

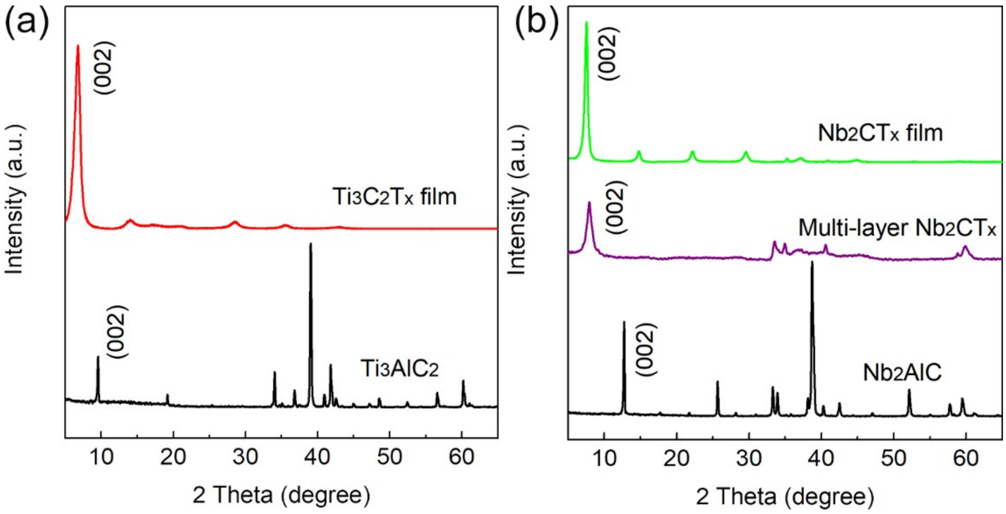

Fig. S6. (a) XRD patterns of Ti_3AlC_2 and pure $Ti_3C_2T_x$ film. (b) XRD patterns of Nb_2AlC and HF-etched multi-layer Nb_2CTx and prepared Nb_2CT_x film.

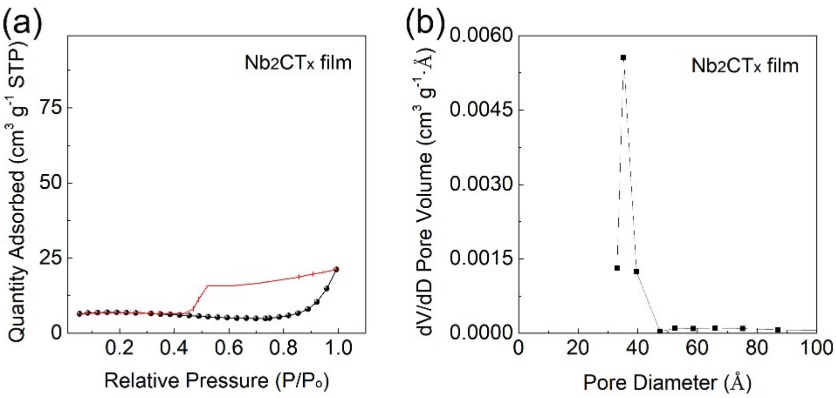

Fig. S7. (a) BET nitrogen adsorption-desorption isotherms and (b) pore size distributions of the Nb_2CT_x film.

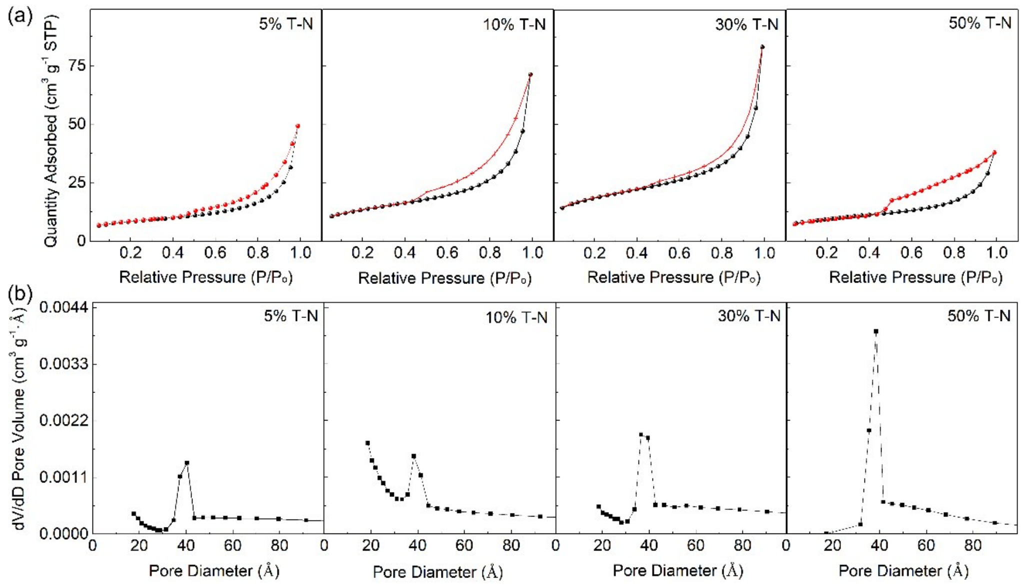

Fig. S8. (a) BET nitrogen adsorption-desorption isotherms of the all-MXene hybrid films, (b) pore size distributions of the all-MXene hybrid films.

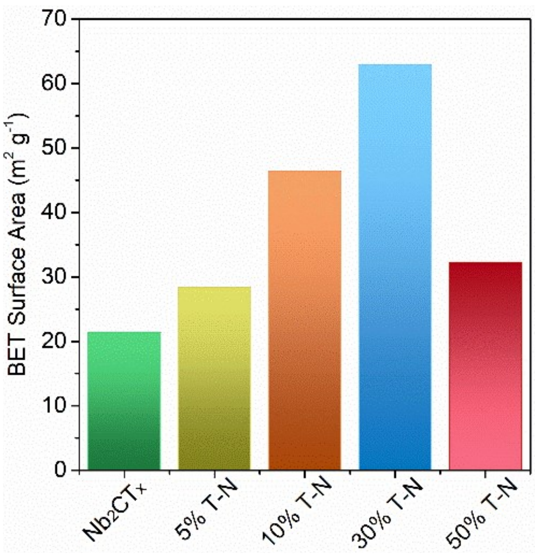

Fig. S9. The BET surface area of the Nb_2CT_x and the all-MXene hybrid films

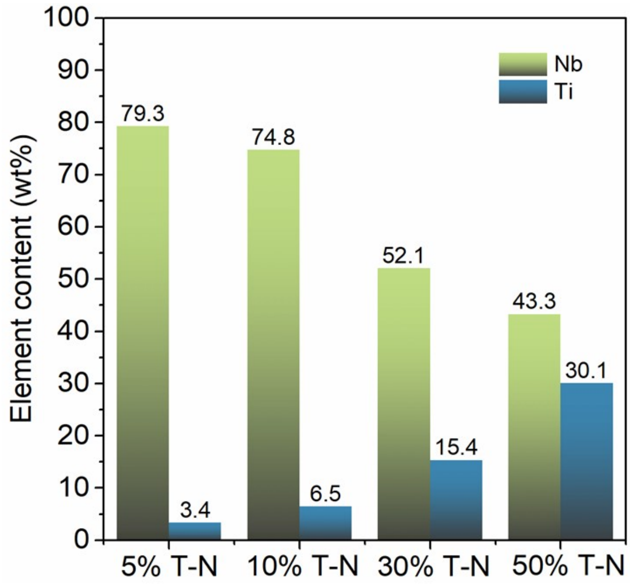

Fig. S10. The Ti and Nb element contents of the all-MXene hybrid films obtained by the ICP analysis.

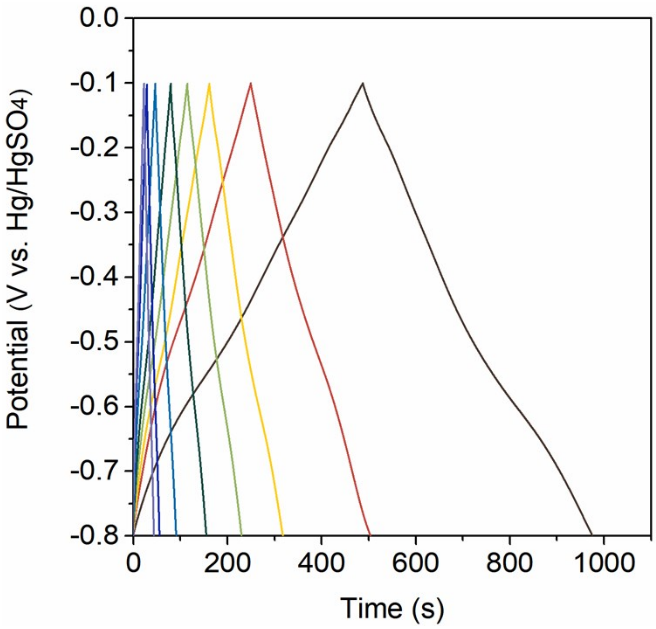

Fig. S11. The GCD curves of 30% T-N at different current densities.

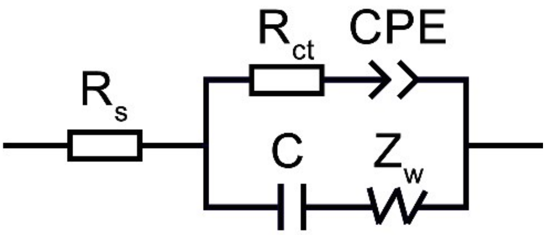

Fig. S12. The electrical equivalent circuit used for fitting impedance spectra. R_s: equivalent series resistance; C: electrical capacitor; R_{ct}: charge transfer resistance; CPE: constant phase angle element, and W: Warburg impedance.

Table S1. Simulation results of the EIS spectra in Fig.4e.

	Nb_2CT_x		5% T-N		10% T-N		30% T-N		50% T-N	
	Values	Error/%	Values	Error/%	Values	Error/%	Values	Error/%	Values	Error/%
R_s/Ohm	7.50	0.73	6.78	0.48	3.87	0.65	3.67	0.96	2.11	0.85
R_{ct}/Ohm	3.46	0.86	2.88	0.62	2.63	0.54	2.52	0.64	2.58	0.82

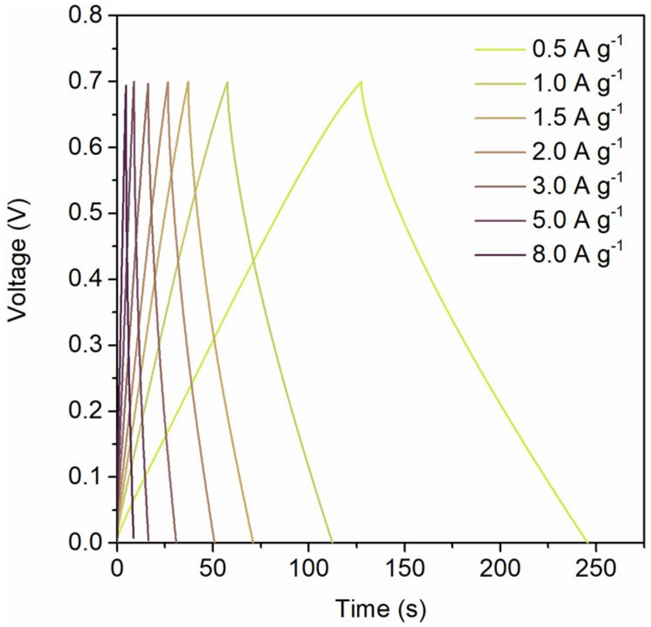

Fig. S13. The GCD curves of 30% T-N based SCs in 2 M H_2SO_4 at different current densities.

Table S2. Comparison of $C_{Gravimetric}$ of the $Ti_3C_2T_x/Nb_2CT_x$ film with the reported MXene-based electrode materials.

Electrode material	**Electrolyte**	**Test condition**	**$C_{gravimetric}$ (F g^{-1})**	**References**
ε-$MnO_2/Ti_3C_2T_x$	30wt% KOH	1 A g^{-1}	210	Ref. 1[1]
$Ti_3C_2T_x$/CNT films	1 M $MgSO_4$	2 mV s^{-1}	150	Ref. 2 [2]
Clay-like $Ti_3C_2T_x$ (thickness: 5 μm)	1 M H_2SO_4	2 mV s^{-1}	245	Ref. 3[3]
d-$Ti_3C_2T_x$ paper	1 M KOH	2 mV s^{-1}	129	Ref. 4[4]
$Ti_3C_2T_x$/ZnO	1 M KOH	2 mV s^{-1}	120	Ref. 5[5]
$Ti_3C_2T_x$/PVA-KOH	1 M KOH	2 mV s^{-1}	168	Ref. 6[6]
$Ti_3C_2T_x$/rGO composite	1 M KOH	2 A g^{-1}	154	Ref. 7[7]
Porous rGO/$Ti_3C_2T_x$ film (thickness: 3 μm)	6 M KOH	1 A g^{-1}	404	Ref. 8[8]
f-$Ti_3C_2T_x$ film (thickness: 3 μm)	1 M KOH	5 mV s^{-1}	140	Ref. 9[9]
V_2CT_x paper (1.9 mg cm^{-2})	1 M H_2SO_4	2 mV s^{-1}	360	Ref. 10[10]
Nb_2CT_x/CNT composite	1 M H_2SO_4	2 mV s^{-1}	202	Ref. 11[11]
$Ti_3C_2T_x$/CNTs	6 M KOH	1 A g^{-1}	134	Ref. 12[12]
Polypyrrole-MXene	1 M H_2SO_4	5 mV s^{-1}	340	Ref. 13[13]
$Ti_3C_2T_x/Nb_2CT_x$ film (thickness: 6 μm)	2 M H_2SO_4	2 mV s^{-1}	370	This Work

Table S3. Comparison of energy density and power density of $Ti_3C_2T_x/Nb_2CT_x$ film based supercapacitors with the previous reported $Ti_3C_2T_x$-based devices.

Material	**Voltage (V)**	**Energy density ($mWh\ g^{-1}$)**	**Power density ($mW\ g^{-1}$)**	**References**
$Ti_3C_2T_x/Nb_2CT_x$ (In 2 M H_2SO_4)	0.7	5.7	172.5	This Work
		2.3	3000.0	
$Ti_3C_2T_x/Nb_2CT_x$ (With PVA-H_2SO_4)	0.7	5.5	141.4	This Work
		1.1	2350.0	
f-$Ti_3C_2T_x$ film	0.4	2.7	49.8	Ref. 12 [14]
d-$Ti_3C_2T_x$ film	0.5	1.4	124.2	Ref. 9 [9]
$Ti_3C_2T_x$/CNTs	0.6	2.8	311.0	Ref. 13 [12]
$Ti_3C_2T_x$ on paper	0.6	0.1	46.6	Ref. 14 [15]
Polypyrrole-MXene	0.6	1.3	41.1	Ref. 15 [13]
3D-print MXene	0.6	2.8	75.3	Ref. 16 [16]

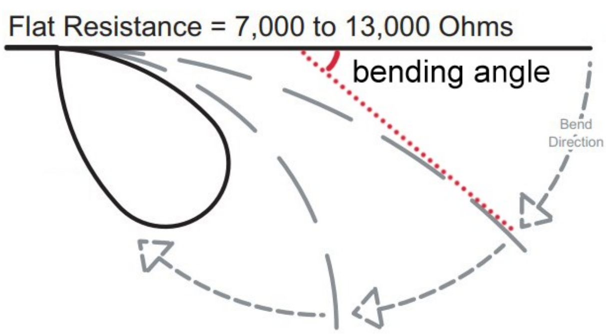

Fig. S14. Schematic diagram of the working principle of the flex sensor

References

1 R. B. Rakhi, B. Ahmed, D. Anjum and H. N. Alshareef, *ACS Appl. Mater. Interfaces,* 2016, ***8,*** 18806-18814.

2 M.-Q. Zhao, C. E. Ren, Z. Ling, M. R. Lukatskaya, C. Zhang, K. L. Van Aken, M. W. Barsoum and Y. Gogotsi, *Adv. Mater.,* 2015, ***27,*** 339-345.

3 M. Ghidiu, M. R. Lukatskaya, M.-Q. Zhao, Y. Gogotsi and M. W. Barsoum, *Nature,* 2014, ***516,*** 78-81.

4 M. R. Lukatskaya, O. Mashtalir, C. E. Ren, Y. Dall'Agnese, P. Rozier, P. L. Taberna, M. Naguib, P. Simon, M. W. Barsoum and Y. Gogotsi, *Science,* 2013, ***341,*** 1502-1505.

5 F. Wang, M. Cao, Y. Qin, J. Zhu, L. Wang and Y. Tang, *RSC Adv.,* 2016, ***6,*** 88934-88942.

6 Z. Ling, C. E. Ren, M.-Q. Zhao, J. Yang, J. M. Giammarco, J. Qiu, M. W. Barsoum and Y. Gogotsi, *Proc. Natl. Acad. Sci. USA,* 2014, ***111,*** 16676-16681.

7 C. Zhao, Q. Wang, H. Zhang, S. Passerini and X. Qian, *ACS Appl. Mater. Interfaces,* 2016, ***8,*** 15661-15667.

8 S. Xu, G. Wei, J. Li, W. Han and Y. Gogotsi, *J. Mater. Chem. A,* 2017, ***5,*** 17442-17451.

9 S. Xu, G. Wei, J. Li, Y. Ji, N. Klyui, V. Izotov and W. Han, *Chem. Eng. J.,* 2017, ***317,*** 1026-1036.

10 Q. Shan, X. Mu, M. Alhabeb, C. E. Shuck, D. Pang, X. Zhao, X.-F. Chu, Y. Wei, F. Du, G. Chen, Y. Gogotsi, Y. Gao and Y. Dall'Agnese, *Electrochem. Commun.,* 2018, ***96,*** 103-107.

11 J. Xiao, J. Wen, J. Zhao, X. Ma, H. Gao and X. Zhang, *Electrochim. Acta,* 2020, ***337,*** 135803.

12 L. Yang, W. Zheng, P. Zhang, J. Chen, W. B. Tian, Y. M. Zhang and Z. M. Sun, *J. Electroanal. Chem.,* 2018, ***830,*** 1-6.

13 J. Yan, Y. Ma, C. Zhang, X. Li, W. Liu, X. Yao, S. Yao and S. Luo, *RSC Adv.,* 2018, ***8,*** 39742-39748.

14 M. Hu, Z. Li, H. Zhang, T. Hu, C. Zhang, Z. Wu and X. Wang, *Chem. Commun.,* 2015, ***51,*** 13531-13533.

15 N. Kurra, B. Ahmed, Y. Gogotsi and H. N. Alshareef, *Adv. Energy Mater.,* 2016, ***6,*** 1601372.

16 W. Yang, J. Yang, J. J. Byun, F. P. Moissinac, J. Xu, S. J. Haigh, M. Domingos, M. A. Bissett, R. A. W. Dryfe and S. Barg, *Adv. Mater.,* 2019, ***31,*** 1902725.